ELSEVIER

Contents lists available at ScienceDirect

## Journal of Food Engineering

journal homepage: www.elsevier.com/locate/jfoodeng





### 3D printing confectionaries with tunable mechanical properties

Ethan Chadwick <sup>a</sup>, Ann H. Barrett <sup>b</sup>, William Hobson-Rhoades <sup>c</sup>, Michael Okamoto <sup>b</sup>, Yara Suleiman <sup>d</sup>, Lauren E. Oleksyk <sup>b</sup>, Hongyi Xu <sup>c</sup>, Sina Shahbazmohamadi <sup>d</sup>, Abhishek Shetty <sup>e</sup>, Richard Baker <sup>f</sup>, Anson W.K. Ma <sup>a,g,\*</sup>

- <sup>a</sup> Department of Chemical and Biomolecular Engineering, University of Connecticut, Storrs, CT, 06269, USA
- <sup>b</sup> DEVCOM Soldier Center, General Greene Ave, Natick, MA, 01760, USA
- <sup>c</sup> Department of Mechanical Engineering, University of Connecticut, Storrs, CT, 06269, USA
- <sup>d</sup> Department of Biomedical Engineering, University of Connecticut, Storrs, CT, 06269, USA
- <sup>e</sup> Rheology Division, Anton Paar USA, 10215 Timber Ridge Dr, Ashland, VA, 23005, USA
- f Integrity Industrial Inkjet Integration, 16 Airpark Rd, West Lebanon, NH, 03784, USA
- g Polymer Program, Institute of Materials Science, University of Connecticut, Storrs, CT, 06269, USA

#### ARTICLE INFO

# Keywords: Additive manufacturing 3D printing Tunable texture Binding mechanism Confectionary

#### ABSTRACT

This paper reports 3D printing of confectionaries using the binder jetting method, where an aqueous binder was printed to selectively join the sugar particles together. Two orders of magnitude difference in compressive strength (from 23 kPa to 1551 kPa) and one order of magnitude difference in elastic modulus (from 1151 kPa to 16,838 kPa) were achieved by adjusting the glycerol concentration of the binder. Such high degree of tunability was attributed to the primary type of bridging (solid versus liquid) between the bound sugar particles. The compressive strength of the 3D printed samples varied between those of a filled hard candy and a marshmallow, although the elastic modulus was at least one order of magnitude higher. Further, a "soft core and hard shell" design was printed and modeled. The discrepancies between experimental and simulation results may be explained by glycerol leaching caused by a glycerol concentration gradient and/or capillary actions.

#### 1. Introduction

3D printing (3DP) refers to the process of building objects layer-wise or dropwise based on a computer-aided design. 3DP is fundamentally different from and complements traditional subtractive manufacturing, where unwanted excess material is removed by cutting, drilling, grinding, to create an object (ISO/ASTM 52900, 2021). In recent years, 3D food printing research has grown exponentially for several reasons. First, 3DP supports the near net shape manufacturing of food products, thereby reducing waste. There is also a growing interest in utilizing by-products from food manufacturing and alternative food source (e.g., insects) as 3DP feedstock (Carvajal-Mena et al., 2022; Feng et al., 2020; Jagadiswaran et al., 2021; Liu et al., 2023). Second, the additive nature of 3DP enables mass customization of food products through texture modulation and personalized nutrition. Texture modulation is desirable for not only satisfying individual preferences and influencing mastication and satiety, but also serving people with dysphagia and elderly who may have difficulties in chewing or swallowing (Diañez et al., 2021; Liu et al., 2023; Pant et al., 2021). Also, unlike molding, 3DP has the flexibility to control the interior structures through different infill patterns and create various shapes without creating a different mold.

Several 3DP technologies have been adapted for food applications (Holland et al., 2018a,b; Rowat et al., 2021). Interested readers are encouraged to read several recent reviews on this topic (Dong et al., 2023; Godoi et al., 2016; Liu et al., 2017; Zhang et al., 2022). Briefly, the most common method is based on material extrusion (MEX), where a paste is prepared and extruded from a nozzle. A wide range of feedstocks have been demonstrated using this method, and the corresponding print process is rather well understood. MEX food printers are commercially available. Powder bed fusion (PBF), using a laser or hot air, has also been demonstrated for sintering or fusing sugar powders (Edman and Oskay, 2014). Binder jetting (BJT) is based on depositing a liquid binder to selectively join particles in a powder bed together. As the ink and powder are supplied separately in the BJT process, BJT does not require the formulation of an extrudable paste as in MEX. BJT complements MEX and is well suited for producing low moisture (<0.85 a<sub>w</sub>) food

<sup>\*</sup> Corresponding author. University of Connecticut, Institute of Materials Science, 25 King Hill Rd Unit 3136, Storrs, CT, 06269, USA. *E-mail address:* anson.ma@uconn.edu (A.W.K. Ma).

products given the relatively small amount of liquid binder used. The room temperature operation of BJT is also beneficial for processing heat sensitive ingredients without compromising the nutritional value.

BJT has been applied to produce lactose-based drug tablets (Chang et al., 2020, 2021; Tan et al., 2023) and selectively crystallize cellulose (Holland et al., 2018a,b). More recently, Zhu and colleagues produced high protein food products from calcium caseinate, highlighting the associated technical challenges (Zhu et al., 2022). Commercially, custom-printed candies are available to order online for special occasions and company marketing. However, with only a few exceptions (Holland et al., 2018a,b; Zhu et al., 2022), most BJT studies focus on the feedstock formulation and final properties of the printed parts. The exact binding mechanism has remained elusive. This study aims to: (i) elucidate the binding mechanism, and (ii) explore how the binding mechanism may be further exploited to modulate the mechanical properties and thus the texture of confectionary products. The mechanical properties of the 3D printed samples have been characterized, modeled, and compared against selected commercial confectionaries that are not 3D printed.

#### 2. Materials and methods

#### 2.1. Sugar powder and characterization

Caster sugar (Judee's Caster Sugar) was obtained from Judee's. Particle size distribution was measured by laser diffraction using the Anton Paar Particle Size Analyzer PSA 1190 equipped with a dry dispersion unit. Results are included in Fig. A1. Powder shear cell experiments were performed using an Anton Paar MCR302 rheometer coupled with the powder shear cell (PSC) accessory (Palmer et al., 2023). The same setup was also used to measure relative volume changes in the sugar sample in response to a load on the sample. Densities at different stresses were calculated based on the compressibility profiles. From this a Hausner ratio ( $HR = \rho_T/\rho_B$ , where  $\rho_T$  is the tapped density and  $\rho_B$  is the bulk density) and Carr Index ( $CI(\%) = 100(1 - \rho_B/\rho_T)$ ) were calculated for different normal stresses (Figs. A2 and A.3). More details can be found in the following references (Chang et al., 2020; Jange et al., 2020; Ramaraju et al., 2022; Zhao et al., 2021).

#### 2.2. Ink preparation and characterization

Kollidon® VA64 (copolymer of 1-vinyl-2-pyrrolidone and vinyl acetate, BASF) was provided in kind by BASF. 99.9% food grade glycerol was obtained from Sigma-Aldrich. Aqueous binders containing different amounts of glycerol, namely, 15%, 30, 45% and 60% (m/v), were prepared by stir-bar mixing for 30 min. The relatively high surface tension of water inhibits jetting, so for the binder containing no glycerol, hereinafter referred to as the "0% glycerol binder", was prepared by adding 5% (m/v) Kollidon® VA64 (KL) to water and mixed for 12 h to reduce the surface tension from 73.3 to 46.9 mN/m, thereby enabling jetting. 1 mL of McCormick Food Dye was added to the binder at 0.2% (v/v) for better visualization of the printed pattern. To remove any foreign particles, all the binder solutions were filtered through a 0.22μm filter paper (Whatman), followed by degassing in a vacuum flask with continuous stirring at 120 rpm for at least 1 h. The viscosity and surface tension of the binders were measured at 25 °C using a cup and bob fixture on a TA Instruments AR-G2 rheometer and the pendant drop method on a DataPhysics OCA 20 goniometer, respectively. The density, viscosity, and surface tension data are included in Table A.1.

#### 2.3. Jetting waveform and amount of jetted binder measurements

The jetting waveform was programmed by the MetWave software (Meteor Inkjet Ltd, Cambridge, UK). A unipolar trapezoidal waveform with a constant rise/fall rate of 39 V/ $\mu$ s, a firing voltage of 135 V, a pulse width of 10  $\mu$ s, and a frequency of 1575 Hz, were selected based on prior work (Chang et al., 2020, 2021; Tan et al., 2023). The amount of binder jetted per print area was calculated by printing a pattern with a known area and weighing the collected binder. Five rounds of jetting were used to increase the total binder amount and reduce the weighing error. The level of binder saturation ( $W_{liquid}$ ) was then calculated by multiplying the amount of binder jetted per print area by the test sample area and the number of print layers.

#### 2.4. 3D printing of test structures

3D printing experiments were performed using a pilot-scale

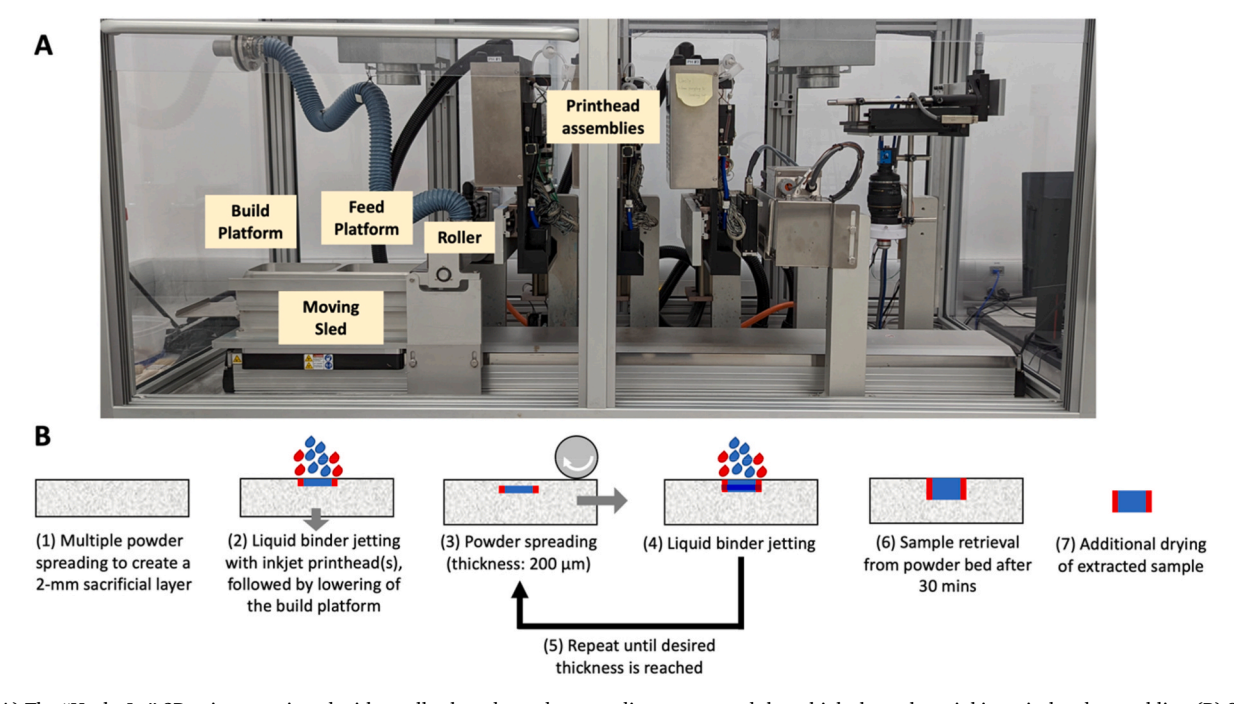


Fig. 1. (A) The "HuskyJet" 3D printer equipped with a roller-based powder spreading system and three high-throughput inkjet printhead assemblies. (B) Schematic diagram of the binder jetting process with the HuskyJet printer.

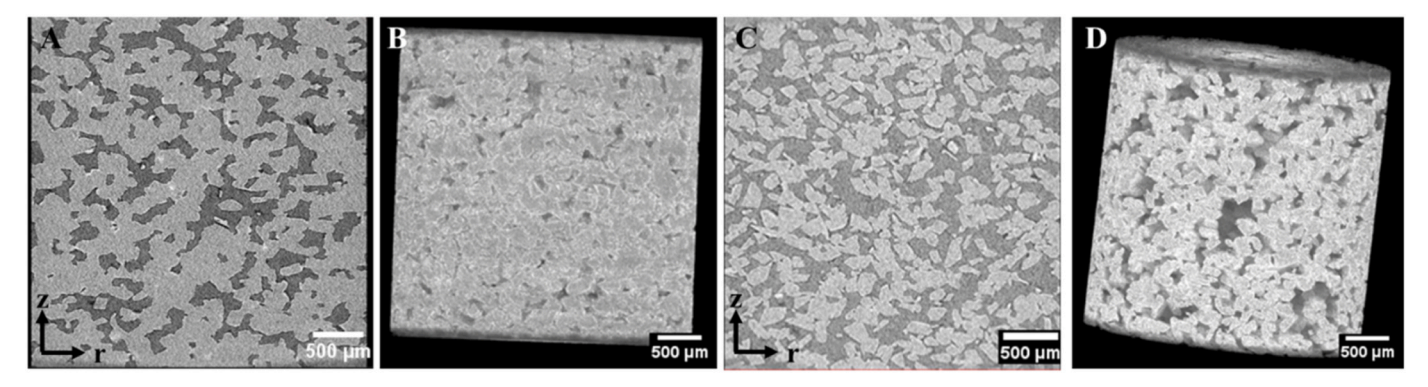


Fig. 2. Micro-CT images of a sample printed with the: (A, B) 0% glycerol binder and (C, D) 60% glycerol binder. (A) and (C) are the cross-sectional images and (B) and (D) are the corresponding images after 3D rendering. Light gray areas show areas of solids while darker regions are voids filled with air or liquid.

HuskyJet 3D printer (Integrity Inkjet Integration, West Lebanon, NH, USA), following the procedure outlined in Fig. 1. The detailed design and operation of the 3D printer were previously reported (Chang et al., 2020, 2021; Tan et al., 2023). The print heads reported in this paper are built for high-throughput printing (e.g., roll-to-roll processing). A similar BJT process has been scaled up for commercial pharmaceutical manufacturing (West and Bradbury, 2018). Appropriate print process parameters were chosen based on prior work (Chang et al., 2020, 2021; Tan et al., 2023). Briefly, caster sugar powder was spread from the feed platform to the build platform as the sled housing both platforms translated at a speed of 100 mm/s under a roller rotating at 120 rpm. The build layer thickness and feed-to-build ratio (= feed layer thickness/build layer thickness) were set to 200 µm and 2, respectively. To prevent the 3D printed structures from sticking to the build platform, ten layers of powders were initially spread onto the build platform without any binder deposition, creating a 2-mm sacrificial layer. The sled then traveled under the printhead(s) that dispensed liquid binder(s). The printer is equipped with three printheads, but only up to two printheads were used in this study. After binder deposition, the sled returned to the initial position. Successive powder spreading and binder deposition were repeated until the entire test structure was printed. Non-core-shell (NCS) structures were printed using a single printhead pre-loaded with a single binder containing a different glycerol concentration. Core-shell (CS) structures were printed sequentially using two printheads — one printhead is pre-loaded with the 0% glycerol binder to create the shell pattern and the other printhead is pre-loaded with a glycerol solution (15%, 30%, 45%, or 60%) for creating the core pattern. A meniscus pressure of 15 psi was applied to prevent the liquid binder from dripping out of the nozzles due to gravity. Both NCS and CS structures are cylinders having a nominal diameter of 15 mm and a nominal thickness of 10 mm. Each batch contained 18 samples and took about 15 min to print. The number of samples per batch may be increased by stacking more samples within the print bed, but increasing the throughput of the process is beyond the scope of this study. The samples were retrieved from the powder bed 30 min after printing, dried for two additional hours under ambient conditions (21 °C, 44% relative humidity). The samples were individually wrapped in lint-free wipes, placed inside centrifuge tubes with a pre-punched hole on the lid, vacuum packed in seal bags with a FoodSaver® vacuum sealer and stored in a cabinet prior to mechanical testing. The size variation from sample to sample is less than 20% and 10% for height and diameter, respectively (Figs. A.4 and A.5).

For CS samples, the percent core area ( $A_{core}$ %) is defined as the cross-sectional area of the core ( $A_{core}$ ) divided by the total cross-sectional area based on the digital design:

$$A_{core}\% = (A_{core} / A_{total}) \times 100\% \tag{1}$$

where  $A_{total}$  was kept constant at 1.767 cm<sup>2</sup>.

Two variables were explored. First, for a constant  $A_{core}\%$  of 50%, the core was printed using a different glycerol binder solution (15%, 30%, 45%, and 60%). Second, for a core printed with the 60% glycerol solution, samples with different  $A_{core}\%$ 's (10%, 25%, 38%, 50%, and 75%) were prepared.

#### 2.5. Microstructure, mechanical and moisture analyses

The microstructure of the 3D printed samples was studied by Microcomputed Tomography (MicroCT; Zeiss Xradia 520 Versa) with ca. 3.5-µm resolution and the following settings (voltage: 60 kV, power: 5 W, exposure: 2s, projections: 1601). Porosity was estimated from micro-CT images using the ImageJ (National Institutes of Health, Bethesda, MD) analysis Toolkit. The images were thresholded to black and white for particles and fluids (air or liquid), respectively, for porosity calculations. The engineering stress/strain data of 3D printed samples were collected using a texture analyzer (TA-XT2, Texture Technologies Corp., Hamilton, MA) equipped with a 50 kg load cell and a 2-cm (dia.) acrylic fixture. The samples were uniaxially compressed at a constant displacement rate of 0.2 mm/s until an engineering strain of 50% was reached. The compressive strength and elastic modulus were calculated from the stress-strain curves. Compressive strength is defined as the peak stress the sample experienced. The elastic modulus is calculated from the slope of the stress-strain curve in the linear regime before yielding. Moisture analysis was performed following the AOAC 934.01 protocol. Briefly, the moisture content was determined by placing the printed samples in a Labconco dryer oven (Model 7,726,500) set at 60 °C for 16 h under vacuum at 25 inHg (0.03 bar). Dried samples were transferred to a desiccator under vacuum at 25 inHg (0.03 bar) where the samples were allowed to cool to room temperature for an hour and weighed. Triplicate measurements were taken and percent moisture on a wet basis was reported.

#### 2.6. Mechanical finite-element modeling

The mechanical properties of various CS structures were modeled using a voxel-based finite element approach. The voxel-based mesh was generated in MathWorks MATLAB (Natick, MA), and then loaded into Dassault Systems ABAQUS (Vélizy-Villacoublay, FR) as a standard explicit simulation. Each voxel is converted to a 0.3125 mm 8-node cubic element (C3D8R, Fig. A6). Each element is assigned with a stress-strain curve using uniaxial Marlow strain energy potential and is susceptible to element deletion for damage evolution. The mechanical properties of the core and shell in each case were determined independently from the experimental data of the NCS structures, considering the maximum, minimum, and median cases. The material input curves for the core and the shell are shown in Fig. A7. The stress-strain curve was simulated as the CS structure was compressed by a plate modeled as a 3D analytic rigid shell to half of its height at a rate of 0.2 mm/s, matching

the experimental test conditions. The bottom layer of the model was constrained in the compression direction only.

#### 2.7. Statistical analysis

At least five samples (n  $\geq$  5) were tested for determining the average mechanical properties. One-way ANOVA tests were performed using Minitab 21 (Minitab, State College, PA) with a significance level of 95% (p < 0.05).

#### 3. Results and discussion

#### 3.1. Powder, liquid binder, and level of binder saturation

In the BJT process, the liquid binder and powder are fed to the printer separately — the liquid binder is dispensed through an inkjet printhead after a layer of the print powder is spread onto the build platform. There are some basic material requirements for the liquid binder and powder, respectively. First, spreading the powder layer uniformly is critical to minimize the unintended formation of macroscale voids that will contribute to sample-to-sample variation and become weak points, reducing the overall strength of the printed structures (Luo et al., 2023; Marczyk et al., 2022). The uniformity of the spread powder layer further depends on the powder flowability and spreading conditions (Chang et al., 2020; Ramaraju et al., 2022). Empirically, the lower the Carr Index (CI) or the Hausner ratio (HR), the higher the flowability. A CI value of less than 5% and a HR value of less than 1.11 indicate excellent flowability (Jange et al., 2020; Ramaraju et al., 2022; Zhao et al., 2021). For the sugar powder used in this study, the CI was measured to be less than 2.2% and the HR was less than 1.023, suggesting the excellent flowability of the sugar powder (Figs. A2 and A.3). These values are considerably lower than those of lactose-based powders that were successfully 3D printed (Chang et al., 2020). According to powder shear cell measurements, the caster sugar powder used in this study is within the "easy flowing" regime, having a flow function coefficient (ff<sub>c</sub>) of 5.7 and 8.3 at consolidation stresses of 1 kPa and 2 kPa, respectively (Palmer et al., 2023). The ffc value determines the extent of flowability in the sample and is inversely related to the cohesivity of powders.

In terms of the liquid binders, Table A1 summarizes the Ohnesorge  $(Oh = \eta/\sqrt{\rho \gamma d})$  numbers calculated from the measured viscosity  $(\eta)$ , density ( $\rho$ ), and surface tension ( $\gamma$ ) of all the liquid binders used, and the nozzle diameter ( $d = 37 \mu m$ ). The *Oh* number physically represents the dimensionless viscosity relative to surface forces and inertia. All the binders have an Oh value less than 1, implying the viscosity is sufficiently low for inkjet printing (Derby, 2010; Guo et al., 2017). Further, the amount of binder jetted, or the level of binder saturation ( $W_{liquid}$ ), is a key parameter in understanding the mechanical properties of the printed samples (Chang et al., 2020; Tan et al., 2023). Table A1 summarizes the measured  $W_{liquid}$  and the normalized glycerol amount  $(W_{glycerol}/W_{sample})$  in the as-printed samples. The total amount of liquid binder dispensed was similar for the glycerol binders, ranging from 90 mg to 117 mg for the chosen jetting waveform. As the glycerol concentration of the liquid binder increased from 15% to 60%, the amount of glycerol deposited was estimated to increase from 0.83% to 2.98% in the as-printed samples.

#### 3.2. Microstructure and binding mechanisms

The 3D printed samples were characterized using micro-CT. Fig. 2 shows the microstructure of samples printed with the 0% glycerol and 60% glycerol binders, respectively. The lighter gray areas correspond to the solid sugar and the darker gray areas are voids filled with air or liquid. The void fraction, or porosity, is estimated to be ca. 28% and ca. 53% for printing with the 0% glycerol binder and the 60% glycerol

binder, respectively. First, as the caster sugar is readily soluble in water, we hypothesize that the exposure of the print powder to the aqueous binders results in the partial dissolution of the sugar particles, forming liquid bridges between the particles. In the absence of glycerol, the water in these liquid bridges further dried out to form solid sugar bridges between the sugar particles. The partial dissolution of the sugar and subsequent formation of solid bridges is proposed to be the primary binding mechanism in samples without glycerol. The proposed mechanism is supported by the clearly observed connectivity between the sugar particles in Fig. 2(A) and (B). For samples printed using the 60% glycerol binder (Fig. 2(C) and (D)), most of the particles appear to be discrete and disconnected. About 3% of glycerol was deposited during printing and 1% of moisture was detected after drying. Liquid bridges between the solid particles may not be clearly visible given their relatively low electron density. These liquid bridges are expected to be weaker than the solid counterparts but will still hold the particles together through capillary forces, resulting in malleable structures and a different sensory texture. The proposed binding mechanisms are schematically illustrated in Fig. 3 and are also supported by the relevant literature of spray dried powder (Adhikari et al., 2001; Hazlett et al., 2021). The binding mechanism may also be explained by the change in the glass transition temperature  $(T_{\sigma})$  of the sugar powders as they are exposed to the aqueous binders.  $T_{\sigma}$  characterizes the transition between the glassy state and rubbery state in amorphous materials. It is well established in the powder caking and agglomeration literature that water increases the molecular mobility of amorphous sugars, thereby reducing the  $T_g$ . Such reduction in  $T_g$  may further: (i) lead to the rubbery state transition of the powders, increasing the overall cohesiveness and/or (ii) induce bridging between powder particles (Cruz-Tirado et al., 2021; Descamps et al., 2013; Fitzpatrick et al., 2007; Foster et al., 2006; Wang and Truong, 2017).

# 3.3. NCS structures: effects of glycerol concentration on mechanical properties

Fig. 4 shows the elastic modulus and compressive strength of NCS structures printed using liquid binders with different glycerol concentrations. Both the elastic modulus and compressive strength exponentially decayed as a function of increasing glycerol concentration in the liquid binder. These results may be explained by the microstructure and binding mechanisms described in Section 3.2. A higher glycerol concentration results in more liquid bridges in the final printed structures. The amount of glycerol deposited was estimated to increase from 0.83% to 2.98% as the glycerol concentration of the binder increased from 15% to 60% (Table A1). The moisture contents of the final dried samples 3D printed with the 0% glycerol, 30% glycerol and 60% glycerol binders were measured to be 0%, 0.7% and 1.07%, respectively. Compared to the solid bridges formed during water evaporation, these liquid bridges are easily deformable and weaker. Samples containing no glycerol were estimated to have a porosity of 25.7% ( = 1 -  $(\rho_{bulk}/\rho_{particle})$ , where  $\rho_{bulk}$ is the bulk density of the printed sample and  $\rho_{particle}$  is the particle density (1.5737 g/cm<sup>3</sup>) (Santos et al., 2018), which is on par with the micro-CT results. As the applied strain exceeded the strain associated with the compressive strength, the measured stress oscillated and progressively decreased (Fig. 4(C)). This is consistent with the stress-strain characteristics of a brittle material, which fails by the sequential collapses of the pores due to local stress concentrations (Gibson and Ashby, 1997). This mode of failure is noticeably different from the glycerol-laden samples, such as that shown in Fig. 4(D) with 60% glycerol as the liquid binder, which tended to exhibit a sharp drop in stress past the compressive strength and then have a small and steady increase in stress after the yield point until the maximum strain is reached. These results suggested that the texture of 3D printed food can be modulated by changing the liquid binder composition and controlling the balance between solid and liquid bridging. However, like non-printed food

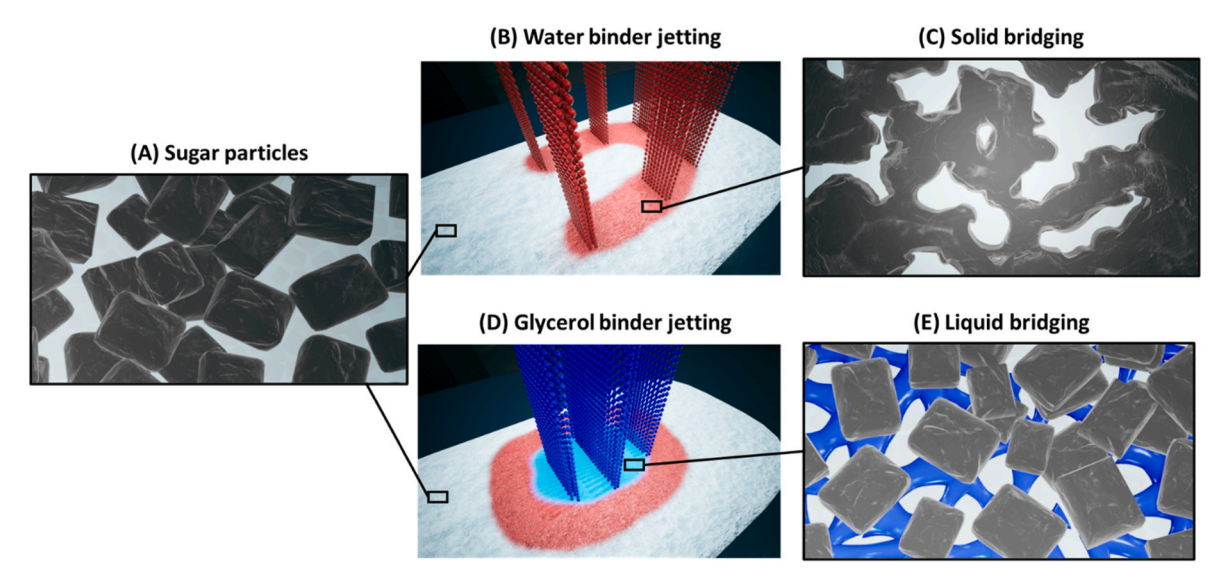


Fig. 3. Proposed binding mechanisms for using a binder with and without glycerol.

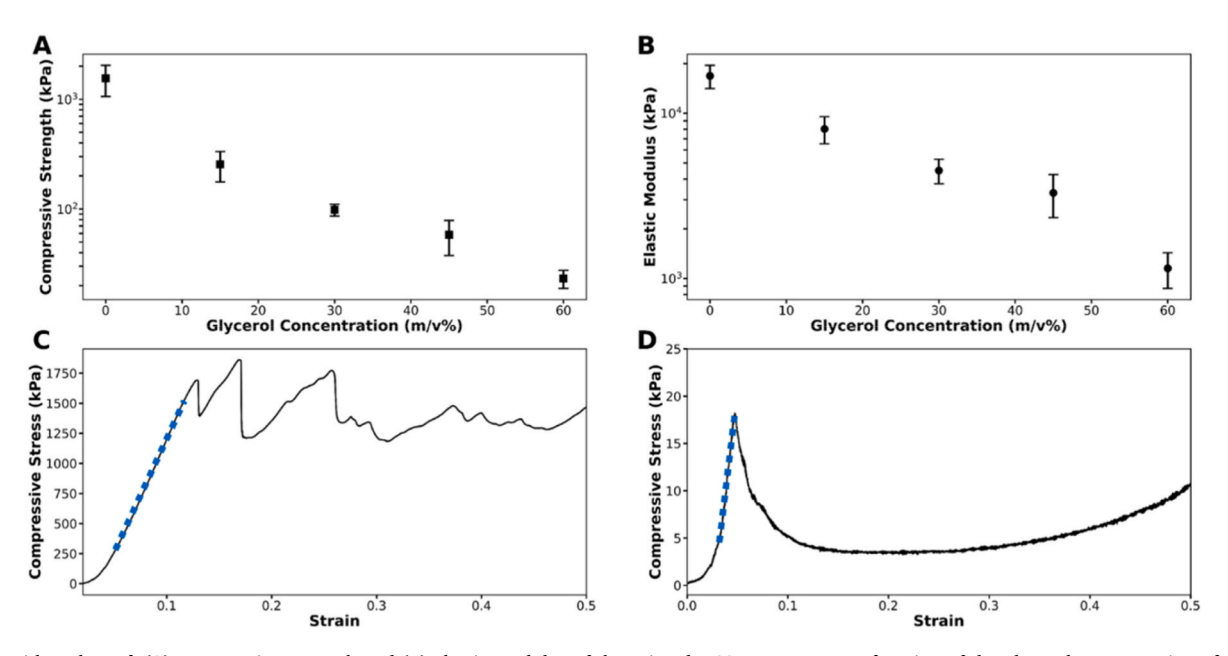


Fig. 4. Semi-log plots of: (A) compressive strength and (B) elastic modulus of the printed NCS structures as a function of the glycerol concentration of the liquid binder. Compressive stress versus strain for samples printed with (C) 0% glycerol and (D) 60% glycerol as the binder, respectively. The blue symbols in (C) and (D) highlight the slopes used for calculating the compressive moduli.

products, appropriate packaging is required to preserve the modulated properties especially if the printed samples are not consumed shortly after production.

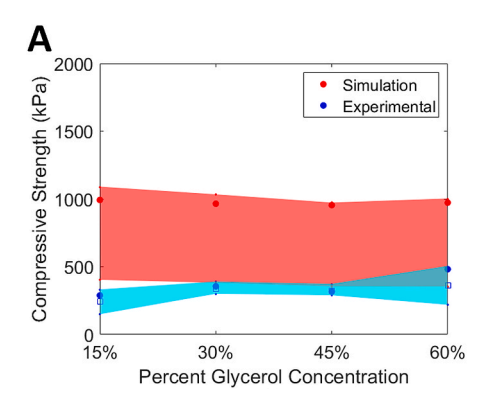
#### 3.4. CS structures: effects of core composition and percent core area

In 3DP, the final shape and structure of the samples can be readily modified by changing the digital design with no need for retooling as in molding. Such flexibility is a key advantage of 3DP that enables mass customization. A wide range of mechanical properties was achieved through the liquid binder containing different glycerol concentrations. In this section, a novel core-shell (CS) design is further explored, where a "soft" core was created with a glycerol solution and a "hard" shell was printed without glycerol. The effects of core composition and percent core area ( $A_{\rm core}\%$ ) on the mechanical properties were modeled and experimentally measured. The simulation results were further compared

against experimental results of the CS structures.

First, Fig. 5(A) compares the predicted compressive strength from simulations with experimentally measured compressive strength as a function of glycerol concentration in the liquid binder for core printing with  $A_{core}\%$  fixed at 50%. Both the simulation and experimental results suggested that despite the relatively large difference in mechanical properties of NCS samples created with different glycerol binders (Fig. 4 (A) and (B)), the CS structures showed only a weak dependence on the core softness. One-way ANOVA (p < 0.05) indicated that the difference in experimentally measured compressive strength is statistically insignificant. Most of the load was carried by the shell until the compressive strength was reached, and changing the core composition has little effect prior to failure.

Second, the effect of core-to-shell ratio was explored by printing CS structures with varying  $A_{\rm core}\%$  (10%, 25%, 38%, 50%, and 75%). All the cores in these samples were printed with the 60% glycerol binder. The



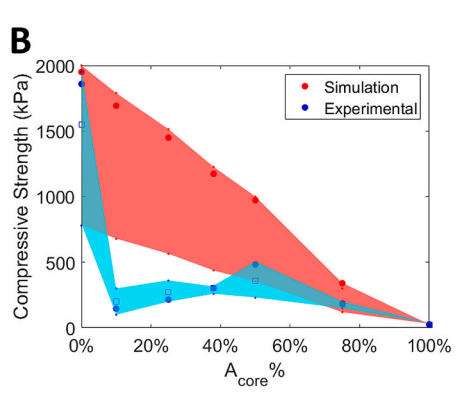


**Fig. 5.** Mechanical properties of 3D printed CS structures: (A) Compressive strength versus glycerol concentration of the binder used for printing the core; (B) Compressive strength versus  $A_{\rm core}$ % for a core printed with the 60% glycerol binder. The filled circle symbols represent the median values, the unfilled squares represent the mean values, and the areas are shaded between the maximum and minimum cases that are: (i) experimentally measured (blue shaded areas) and (ii) simulated (red shaded areas) using the experimental maximum and minimum properties of the NCS samples as model inputs.

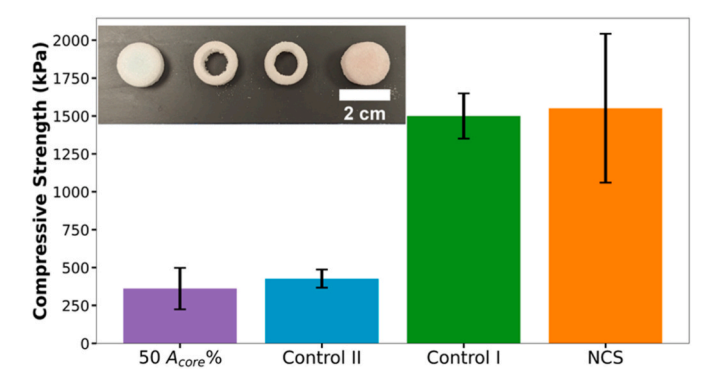


**Fig. 6.** Compressive strength of two control (Control I and Control II) and two non-control samples (50  $A_{core}$ % and NCS). For "Control I" samples, only the shell was printed with the 0% glycerol binder. For "Control II" samples, a 50% area core was printed using the 60% glycerol binder but removed manually 1 h after printing and discarded. "50  $A_{core}$ %" refers to CS samples that are the same as Control II samples except that the core has not been removed. "NCS" refers to NCS samples printed entirely with the 0% glycerol binder. Error bars represent standard deviations.

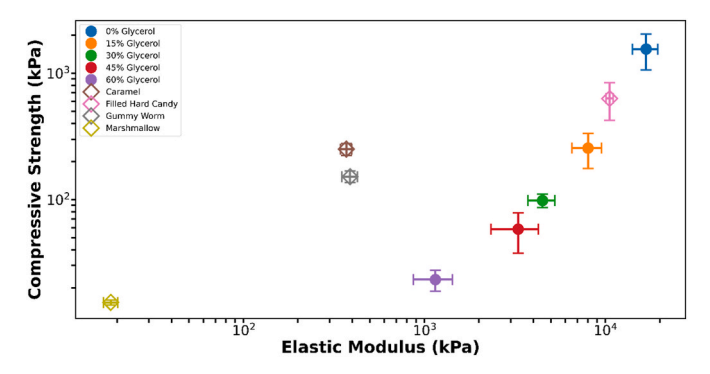


**Fig. 7.** Log-log plot of compressive strength and elastic modulus of 3D printed samples versus commercial products that are not 3D printed. The commercial samples are: Arcor filled hard candy, Arcor caramel, Black Forest gummy worm, and Amazon Happy Belly marshmallow. The compressive strengths of caramel, gummy worm and marshmallow were taken as the measured stresses at 50% strain due to the samples not failing.

limiting cases of  $A_{\rm core}\%=0\%$  and  $A_{\rm core}\%=100\%$  correspond to the NCS samples printed fully with the 0% glycerol and 60% glycerol binders, respectively. The close agreements between experimental and simulation results in these limiting cases confirm the method of extracting material properties of the core and shell independently from the NCS data is adequate. The average compressive strength has reduced significantly from 1551 kPa (with no core) to 200 kPa for 10% core area.

All the CS structures have an average compressive strength between that of a NCS sample printed with 0% glycerol and a NCS sample printed entirely with 60% glycerol, but the difference in the measured compressive strengths among the CS samples with different percent core areas are statistically insignificant based on a one-way ANOVA (p < 0.05). Two discrepancies between the experimental and simulation results are noted. First, in Fig. 5(A), the model consistently predicted a higher compressive strength compared to the experimental data. Second, in Fig. 5(B), the model predicted that the compressive strength would decrease monotonically, which was not observed experimentally.

We hypothesize that the glycerol solution has leached from the core to the shell, consequently weakening the shell. To examine this hypothesis, two types of control samples were prepared based on the 50% core area design. In one type of control samples ("Control I"), only the shell was printed. In another type of control samples ("Control II"), the core was printed using the 60% glycerol binder, but removed manually and discarded 1 h after the samples were recovered from the powder bed, leaving the shell for further drying. Fig. 6 shows the images and corresponding mechanical properties of these two different types of control samples next to a "50 A<sub>core</sub>%" CS sample having a 50% area core printed with the 60% glycerol binder and a "NCS" sample printed using the 0% glycerol binder. For Control I samples, the compressive strength was comparable to the NCS sample but was significantly higher than the  $50~A_{core}\%$  sample and Control II. For Control II samples, the compressive strength was comparable to the 50 Acore% sample, but lower than Control I. These findings support the hypothesis that the glycerol in the core has diffused into the shell and consequently weakened the shell. Mechanically, the diffusion of glycerol into the shell may also result in a "slip boundary", where the outer shell may slide off and separate from the core instead of being fully compressed. A practical implication of this finding is that if liquid bridges are used to modulate the overall mechanical properties, the mobility of these bridges and possible mass transfer in the as-printed structures must be considered. There are two possible mechanisms for the mass transfer to occur. First, soon after the two different binder solutions are deposited in the core and the shell separately, there exists a solution concentration gradient that may lead to the diffusion from the core with a higher glycerol concentration to the shell with a lower glycerol concentration (Bird et al., 2006). Second, as the shell continues to dry at a faster rate than the core, the newly formed pores may draw the glycerol solution from the core region through capillary actions (Norman R. Morrow, 1970).

## 3.4. Tunable mechanical properties and benchmarking against commercial products

The measured elastic modulus and compressive strength for the different NCS structures 3D printed in this study were plotted against four commercial products that are not 3D printed (Fig. 7). For the NCS samples, a wide range of mechanical properties was achieved by varying the binder composition. The elastic modulus of the samples 3D printed

from caster sugar powder was at least an order of magnitude higher than the non-printed samples, except for the filled hard candy. The compressive strength and elastic modulus of the filled hard candy were between that of the 0% glycerol and 15% glycerol NCS samples. Compared to the NCS structures, CS structures have a lower elastic modulus and compressive strength that tend to cluster around the 15% glycerol NCS samples (Fig. A.11). It is evident, then, changing the core composition and percent core area only have moderate impact on the overall mechanical properties which are dominated by the harder shell; however, the strength of the shell is affected by glycerol leaching from the core probably because of a glycerol concentration gradient and/or capillary actions.

#### 4. Conclusions

This paper reports 3D printing of confectionaries with tunable texture using the binder jetting method with caster sugar as the base powder and various liquid binders containing different glycerol concentrations. The compressive strength and elastic modulus of the 3D printed samples strongly depended on the glycerol amount in the liquid binder. Samples printed without glycerol fractured as a brittle material, whereas the samples with glycerol exhibited clear plastic deformation with non-oscillating stress-strain functions and continued to be compacted following initial failure. Increasing the amount of glycerol in the liquid binder progressively reduced the compressive strength by up to two orders of magnitude and the elastic modulus by up to one order of magnitude. Such a wide range of tunable mechanical properties is attributed to the primary binding mechanism — solid versus liquid bridging between sugar particles. The second part of this paper investigated a new type of "soft core and hard shell" structures. Two design parameters, namely, the core composition and the percent core area, were explored. Changing the glycerol amount in the liquid binder for printing the core had little effect on the overall compressive strength and elastic modulus. In terms of percent core area, inclusion of a core as small as 10% considerably weakened the entire structures, probably caused by glycerol leaching into the shell due to a glycerol concentration gradient and/or capillary actions. Lastly, the 3D printed samples were compared against several commercial confectionary products. The compressive strength of the 3D printed samples varied between that of a hard candy and marshmallow, but the elastic modulus was generally higher. For the relatively simple cylindrical test structures studied in this paper, changing the liquid binder composition in a non-core-shell design is more effective in modulating the mechanical properties compared to varying the core-shell design.

#### Author credit statement

Ethan Chadwick: Methodology, Formal Analysis, Investigation, Validation, Writing – Original Draft, Writing – Review & Editing, Visualization Ann H. Barrett: Investigation, Formal analysis, Writing – Review & Editing; William Hoboson-Rhoades: Investigation, Writing – Original Draft, Visualization Michael Okamoto: Investigation, Formal analysis, Writing – Review & Editing Yara Suleiman: Investigation, Writing – Original Draft, Visualization Lauren E. Oleksyk: Funding Acquisition, Supervision Hongyi Xu: Methodology, Supervision Sina Shahbazmodamadi: Supervision, Resources Abhishek Shetty: Investigation, Writing – Original Draft, Writing – Review & Editing, Resources Richard Baker: Conceptualization Anson W. K. Ma: Conceptualization, Methodology, Writing – Original Draft, Writing – Review & Editing, Supervision, Project administration, Funding acquisition.

#### **Declaration of competing interest**

The authors declare that they have no known competing financial interests or personal relationships that could have appeared to influence the work reported in this paper.

#### Data availability

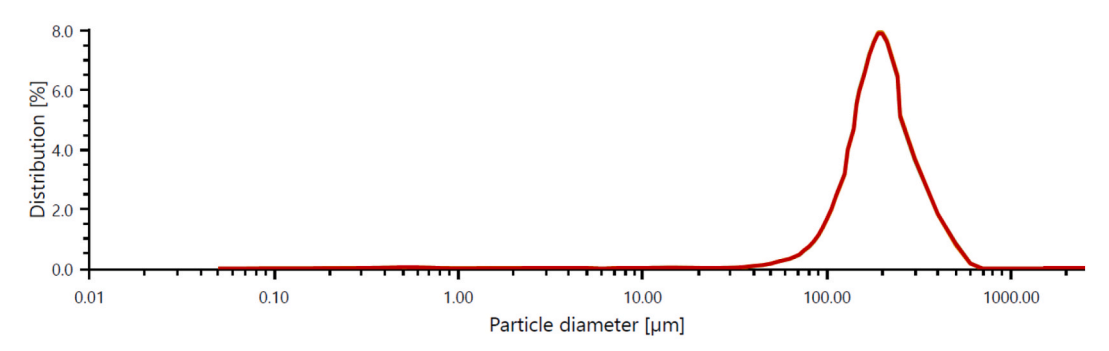
Data will be made available on request.

#### Acknowledgements

The authors would like to acknowledge BASF for providing in-kind samples, Prof. Yangchao Luo for offering access to a texture analyzer, and Danial Ezzati for creating the graphics for illustrating the binding mechanisms. This work is partly supported by: (i) the USDA National Institute of Food and Agriculture, AFRI project 2019–06721 (under Grant No. 2020-67017-31273) and (ii) the National Science Foundation under Grant No. IIP-#1822157 (Phase I IUCRC at University of Connecticut: Center for Science of Heterogeneous Additive Printing of 3D Materials (SHAP3D). Any opinions, findings, and conclusions or recommendations expressed in this material are those of the author(s) and do not necessarily reflect the views of the National Science Foundation or the sponsors.

#### Appendix

#### Distribution (volume)



Statistics (volume) - Undersize									
	Name	D <sub>10</sub> [μm]	D₅₀ [μm]	D <sub>90</sub> [μm]	Mean size [μm]	Span			
	Mean value	103.125	183.061	304.423	208.080	1.100			
	Standard deviation	0.3428	0.2140	1.8918	0.2301	0.012			
	Rel. standard deviation	0.33	0.12	0.62	0.11	1.08			

Fig. A.1. Particle size distribution of Judee's Caster Sugar.

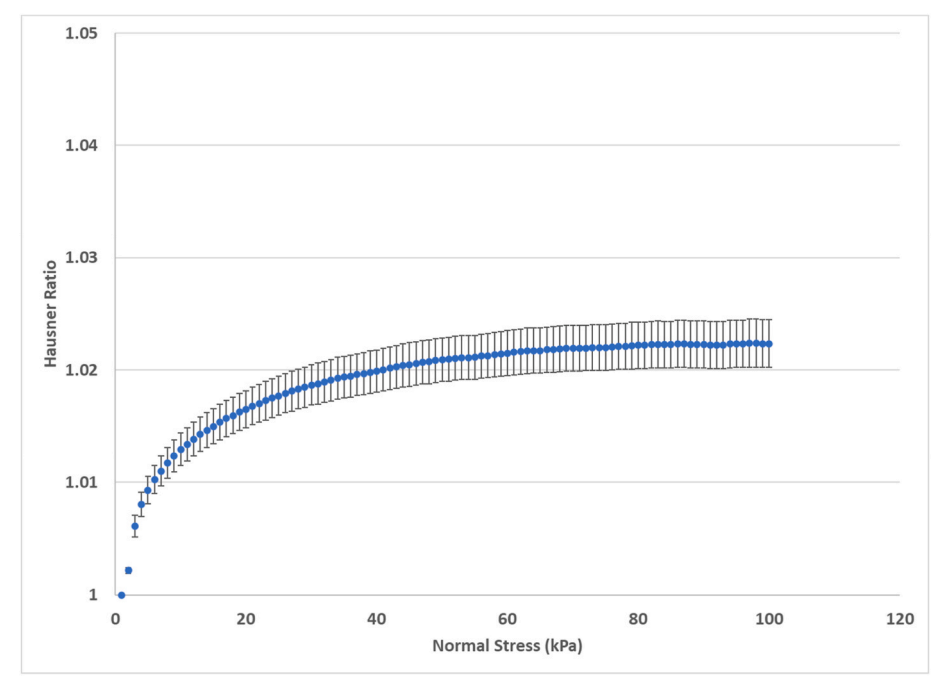


Fig. A.2. Hausner Ratio (HR) as a function of applied normal stress.

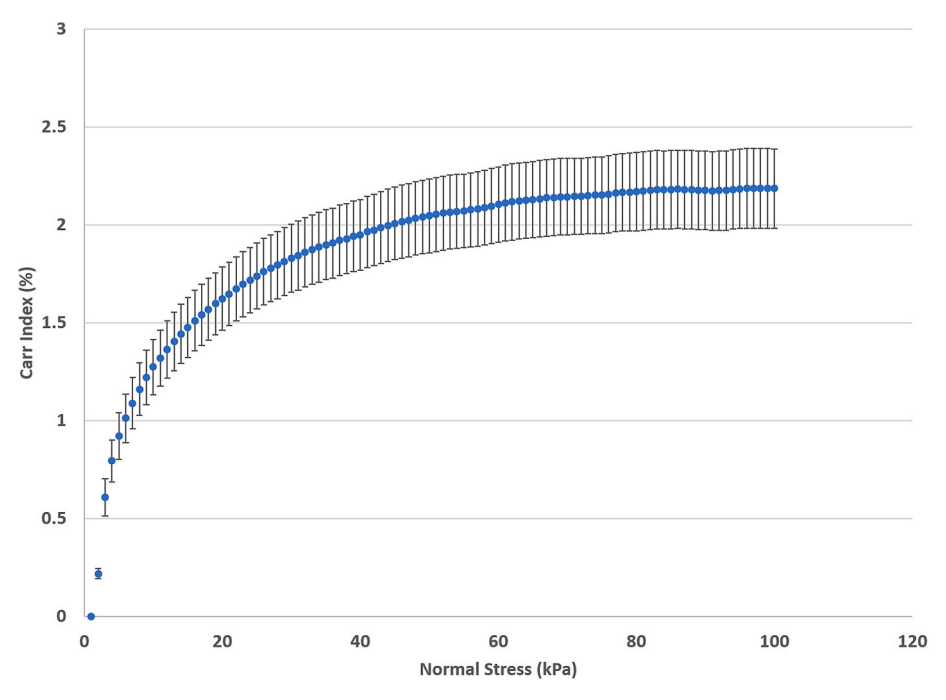


Fig. A.3. Carr Index (CI) as a function of applied normal stress.

Table A.1
Density, viscosity, surface tension, Ohnesorge (Oh) number of the liquid binders, and for each as-printed sample, the measured level of binder saturation ( $W_{liquid}$ ), and glycerol amount ( $W_{glycerol}$ ) normalized by the average sample mass ( $W_{sample}$ ). Shear rate: 10 s<sup>-1</sup>; Temperature: 25 °C.

Glycerol Conc.	Density (kg/m <sup>3</sup> )	Viscosity (mPa s)	Surface Tension (mN/m)	Oh	$W_{liquid}$ (mg)	$\frac{W_{glycerol}}{W_{sample}}$ (%)
0%	1007	3.5	46.90	0.081	197	0
15%	1050	1.52	71.33	0.028	111	0.83
30%	1087	2.45	68.46	0.045	117	1.72
45%	1126	4.41	65.94	0.081	90	2.12
60%	1166	10	65.14	0.181	107	2.98

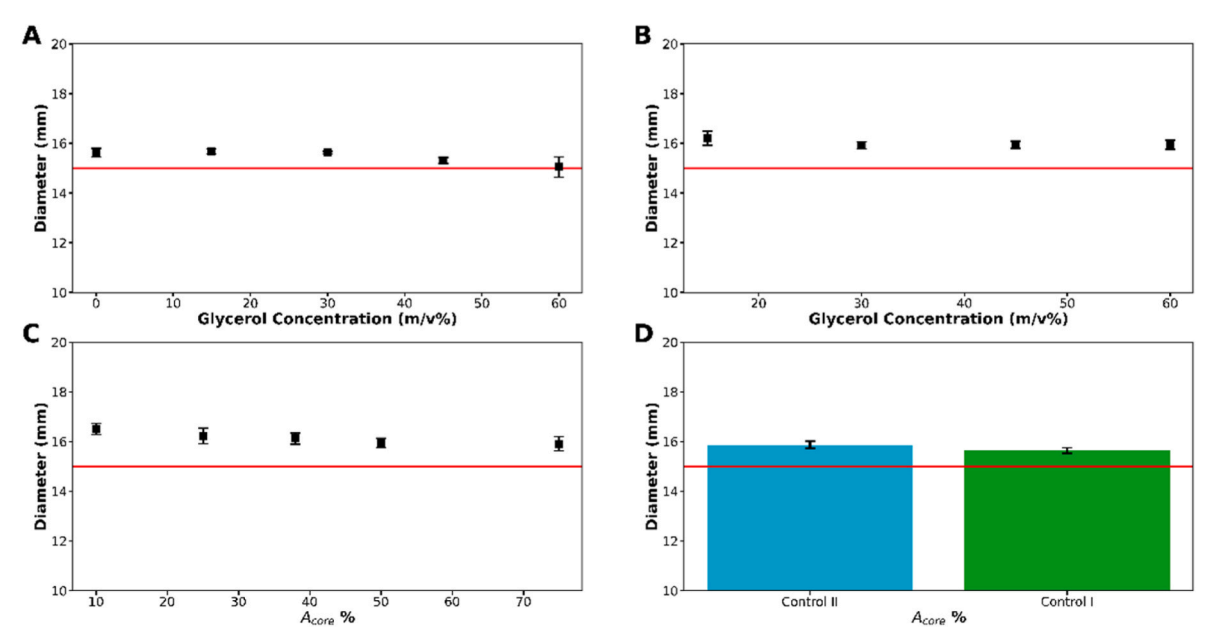


Fig. A.4. Measured diameters of: (a) NCS structures printed using different binders, (b) CS structures with the core printed using a different binder and a fixed  $A_{core}$ % of 50%, (c) CS structures with varying  $A_{core}$ %, where the shell was printed using the 0% glycerol binder and the core was printed using the 60% glycerol binder, (d) diameters of Control I and II. The red lines indicate the target diameter of 15 mm. Error bars represent standard deviations.

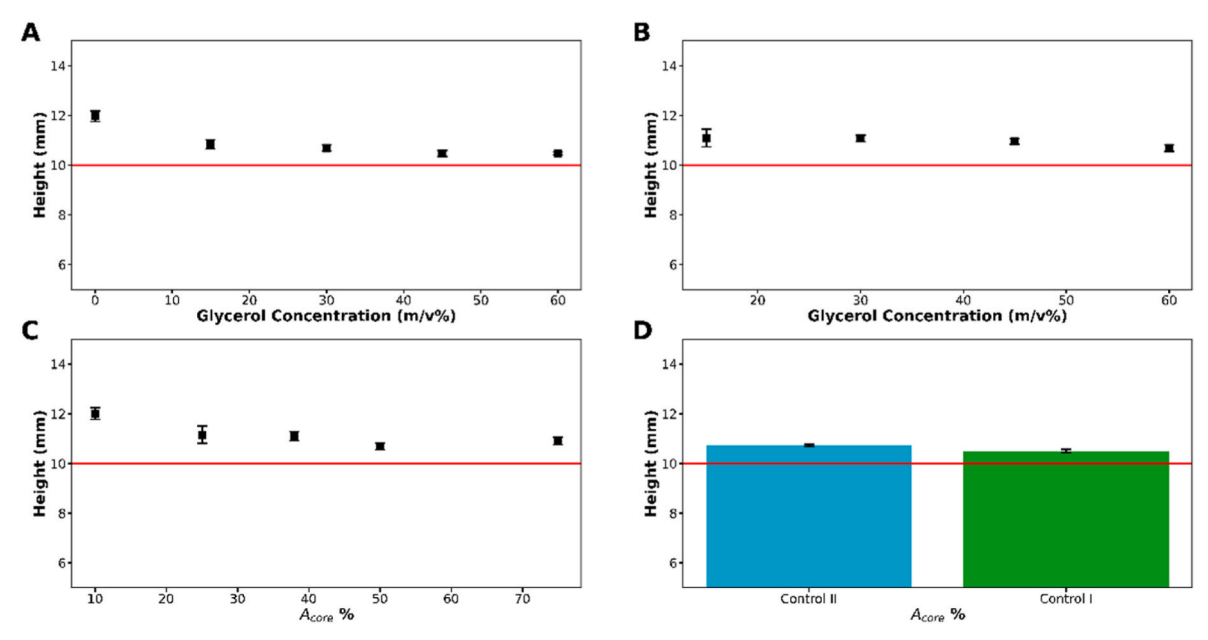
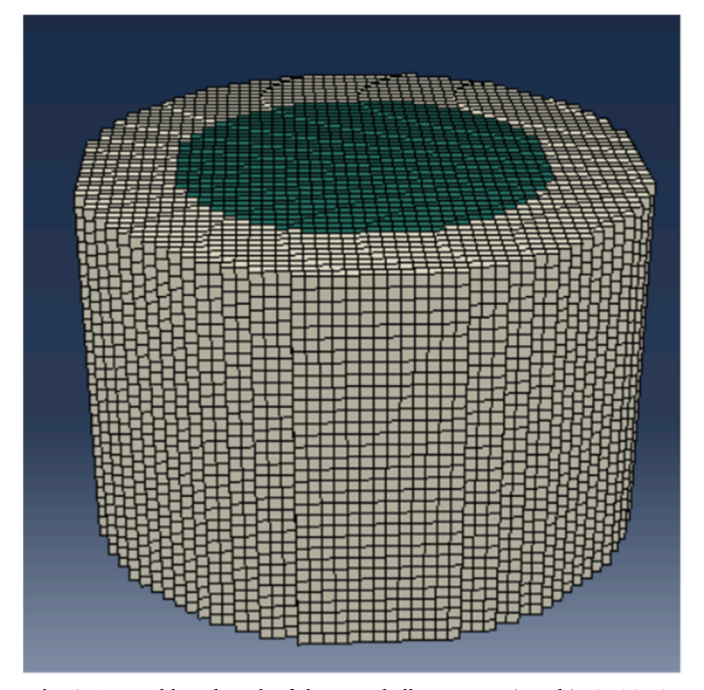


Fig. A.5. Measured heights of: (a) NCS structures printed using different binders, (b) CS structures with the core printed using a different binder and a fixed  $A_{core}$ % of 50%, (c) CS structures with varying  $A_{core}$ %, where the shell was printed using the 0% glycerol binder and the core was printed using the 60% glycerol binder, (d) diameters of Control I and II. The red lines indicate the target height of 10 mm. Error bars represent standard deviations.



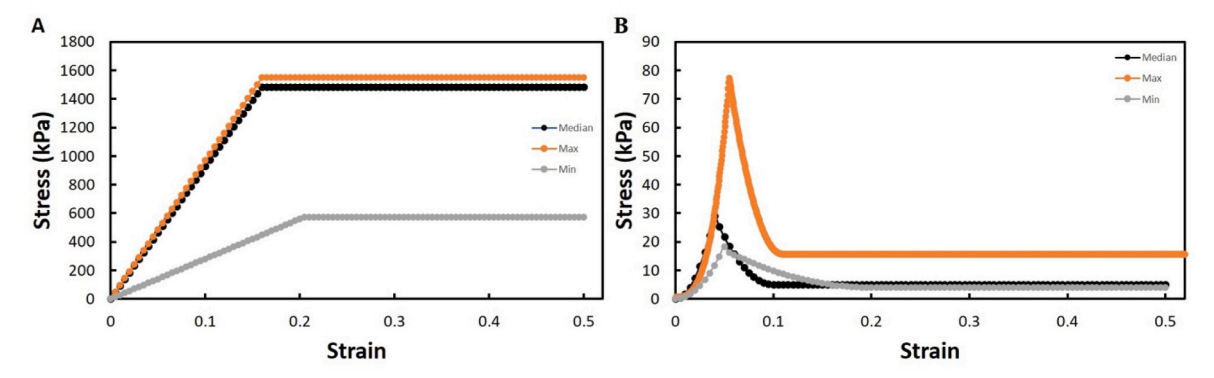


Fig. A.7. Example material input curves used in finite element modeling for: (a) a shell printed with 0% glycerol and (b) a core printed with 60% glycerol.

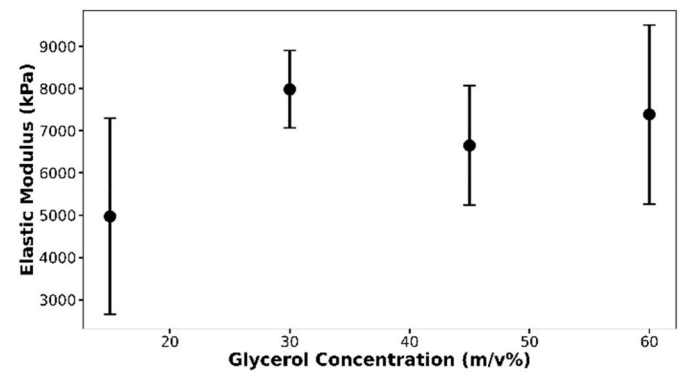


Fig. A.8. Compressive elastic modulus versus glycerol concentration of the binder used for printing the core for a fixed  $A_{core}\%$  of 50%. Error bars represent standard deviations.

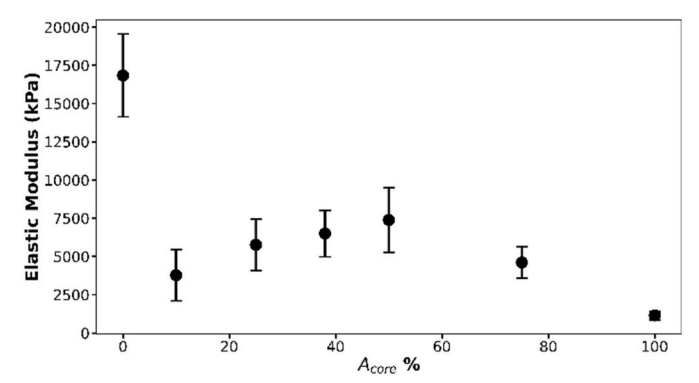


Fig. A.9. Compressive elastic modulus versus  $A_{core}$ % for a core printed with the 60% glycerol binder and a shell printed with the 0% glycerol binder. Error bars represent standard deviations.

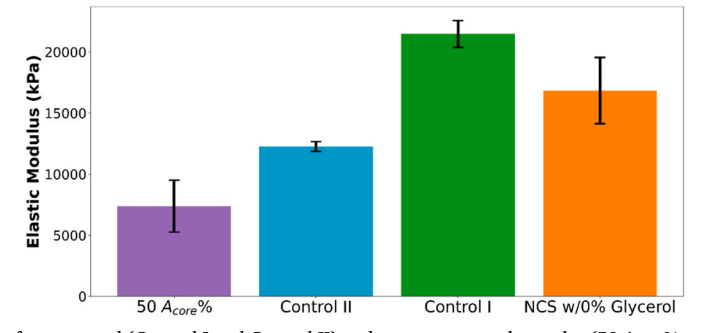


Fig. A.10. Compressive elastic modulus of two control (Control I and Control II) and two non-control samples (50  $A_{core}$ % and NCS). For "Control I" samples, only the shell was printed with the 0% glycerol binder. For "Control II" samples, a 50% area core was printed using the 60% glycerol binder but removed manually and discarded 1 h after printing. "50  $A_{core}$ %" samples are CS samples that are the same as Control II samples except that the core has not been removed. "NCS" are NCS samples printed entirely with the 0% glycerol binder. Error bars represent standard deviations.

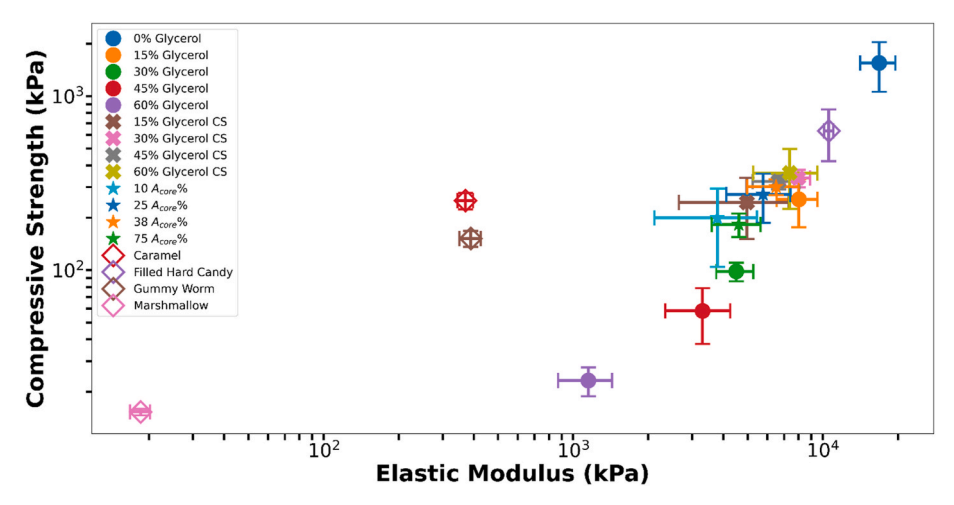


Fig. A.11. Compressive strength and elastic modulus of all 3D printed samples in this work versus commercial products that are not 3D printed. The samples are: Arcor filled hard candy, Arcor caramel, Black Forest gummy worm, and Amazon Happy Belly marshmallow. The compressive strengths for the caramel, gummy worm, and marshmallow values were taken as the stresses measured at the maximum applied strain of 50% due to the samples not failing.

#### References

Adhikari, B., Howes, T., Bhandari, B.R., Truong, V., 2001. Stickiness in foods: a review of mechanisms and test methods. Int. J. Food Prop. 4 (1), 1–33.

Bird, R.B., Stewart, W.E., Lightfoot, E.N., 2006. Transport Phenomena. Wiley, 2<sup>nd</sup> eds. Carvajal-Mena, N., Tabilo-Munizaga, G., Pérez-Won, M., Lemus-Mondaca, R., 2022. Valorization of salmon industry by-products: evaluation of salmon skin gelatin as a biomaterial suitable for 3D food printing. Lebensm. Wiss. Technol. 155, 112931.

Chang, S., Jin, J., Yan, J., Dong, X., Chaudhuri, B., Nagapudi, K., Ma, A.W.K., 2021. Development of a pilot-scale HuskyJet binder jet 3D printer for additive manufacturing of pharmaceutical tablets. Int. J. Pharm. 605, 120791.

Chang, S., Li, S.W., Kowsari, K., Shetty, A., Sorrells, L., Sen, K., Nagapudi, K., Chaudhuri, B., Ma, A.W.K., 2020. Binder-Jet 3D printing of Indomethacin-laden pharmaceutical dosage forms. J. Pharmaceut. Sci. 109 (10), 3054–3063.

Cruz-Tirado, J.P., Martins, J.P., Olmos, B.D.F., Condotta, R., Kurozawa, L.E., 2021. Impact of glass transition on chemical properties, caking and flowability of soymilk powder during storage. Powder Technol. 386, 20–29.

Derby, B., 2010. Inkjet printing of functional and structural materials: fluid property requirements, feature stability, and resolution. Annu. Rev. Mater. Res. 40 (1), 395–414.

Descamps, N., Palzer, S., Roos, Y.H., Fitzpatrick, J.J., 2013. Glass transition and flowability/caking behaviour of maltodextrin DE 21. J. Food Eng. 119 (4), 809–813.

Diañez, I., Gallegos, C., Brito-de la Fuente, E., Martínez, I., Valencia, C., Sánchez, M.C., Franco, J.M., 2021. Implementation of a novel continuous solid/liquid mixing accessory for 3D printing of dysphagia-oriented thickened fluids. Food Hydrocolloids 120, 106900.

Dong, H., Wang, P., Yang, Z., Xu, X., 2023. 3D printing based on meat materials: challenges and opportunities. Curr. Res. Food Sci. 6, 100423.

Edman, L., Oskay, W., 2014. The CandyFab Project, p. 2023. April 4th.

Feng, C., Zhang, M., Bhandari, B., Ye, Y., 2020. Use of potato processing by-product: effects on the 3D printing characteristics of the yam and the texture of air-fried yam snacks. Lebensm. Wiss. Technol. 125, 109265.

Fitzpatrick, J.J., Hodnett, M., Twomey, M., Cerqueira, P.S.M., O'Flynn, J., Roos, Y.H., 2007. Glass transition and the flowability and caking of powders containing amorphous lactose. Powder Technol. 178 (2), 119–128.

Foster, K.D., Bronlund, J.E., Paterson, A.H.J., 2006. Glass transition related cohesion of amorphous sugar powders. J. Food Eng. 77 (4), 997–1006.

Gibson, L.J., Ashby, M.F., 1997. Cellular Solids: Structure and Properties, second ed.s. Cambridge University Press, Cambridge.

Godoi, F.C., Prakash, S., Bhandari, B.R., 2016. 3D printing technologies applied for food design: status and prospects. J. Food Eng. 179, 44–54.

Guo, Y., Patanwala, H.S., Bognet, B., Ma, A.W.K., 2017. Inkjet and inkjet-based 3D printing: connecting fluid properties and printing performance. Rapid Prototyp. J. 23 (3), 562–576.

Hazlett, R., Schmidmeier, C., O'Mahony, J.A., 2021. Approaches for improving the flowability of high-protein dairy powders post spray drying – a review. Powder Technol. 388, 26–40.

Holland, S., Foster, T., MacNaughtan, W., Tuck, C., 2018a. Design and characterisation of food grade powders and inks for microstructure control using 3D printing. J. Food Eng. 220, 12–19.

Holland, S., Tuck, C., Foster, T., 2018b. Selective recrystallization of cellulose composite powders and microstructure creation through 3D binder jetting. Carbohydr. Polym. 200, 229–238.

ISO/ASTM 52900, 2021. Additive Manufacturing -General Principles - Fundamentals and Vocabulary 1,2. ISO/ASTM 52900:2021(E). Jagadiswaran, B., Alagarasan, V., Palanivelu, P., Theagarajan, R., Moses, J.A., Anandharamakrishnan, C., 2021. Valorization of food industry waste and byproducts using 3D printing: a study on the development of value-added functional cookies. Future Foods 4, 100036.

Jange, C.G., Taku, P., Peng, S., Dixon, M.P., Shetty, A., Ambrose, R.P.K., 2020. Cohesivity assessment of semi-crystalline and crystalline powders using a Warren Springs cohesion tester. Powder Technol. 371, 96–105.

Liu, Z., Xing, X., Mo, H., Xu, D., Hu, L., Li, H., Chitrakar, B., 2023. 3D printed dysphagia diet designed from Hypsizygus marmoreus by-products with various polysaccharides. J. Food Eng. 343, 111395.

polysaccharides. J. Food Eng. 343, 111395.
Liu, Z., Zhang, M., Bhandari, B., Wang, Y., 2017. 3D printing: printing precision and application in food sector. Trends Food Sci. Technol. 69, 83–94.

Luo, W., Fang, Z., Ma, C., Wu, M., Zhuo, Z., 2023. Ball milling treatment of Nb and B nanoparticles modified TiAl4822 composite powder and its effect on powder bed quality and powder spreadability in additive manufacturing. Adv. Eng. Mater., 2200846

Marczyk, J., Ostrowska, K., Hebda, M., 2022. Influence of binder jet 3D printing process parameters from irregular feedstock powder on final properties of Al parts. Adv. Powder Technol. 33 (11), 103768.

Morrow, N.R., 1970. Physics and thermodynamics of capillary action in porous media. Ind. Eng. Chem. 62 (6), 32–56.

Palmer, K., Parhi, A., Shetty, A., Sunkesula, V., Sharma, P., 2023. Development of methodology for assessing flowability of milk protein powders using shear failure testing device. J. Food Eng. 348, 111450.

Pant, A., Lee, A.Y., Karyappa, R., Lee, C.P., An, J., Hashimoto, M., Tan, U., Wong, G., Chua, C.K., Zhang, Y., 2021. 3D food printing of fresh vegetables using food hydrocolloids for dysphagic patients. Food Hydrocolloids 114, 106546.

Ramaraju, H., Landry, A.M., Sashidharan, S., Shetty, A., Crotts, S.J., Maher, K.O., Goudy, S.L., Hollister, S.J., 2022. Clinical grade manufacture of 3D printed patient specific biodegradable devices for pediatric airway support. Biomaterials 289, 121702.

Rowat, S.J., Legge, R.L., Moresoli, C., 2021. Plant protein in material extrusion 3D printing: formation, plasticization, prospects, and challenges. J. Food Eng. 308, 110623.

Santos, L.C.d., Condotta, R., Ferreira, M.d.C., 2018. Flow properties of coarse and fine sugar powders. J. Food Process. Eng. 41 (2), e12648.

Tan, M., Dharani, D., Dong, X., Maiorana, C., Chaudhuri, B., Nagapudi, K., Chang, S., Ma, A.W.K., 2023. Pilot-scale binder jet 3D printing of sustained release solid dosage forms. Int. J. Pharm. 631, 122540.

Wang, Y., Truong, T., 2017. Chapter 7 - glass transition and crystallization in foods. In: Bhandari, B., Roos, Y.H. (Eds.), Non-equilibrium States and Glass Transitions in Foods. Woodhead Publishing, pp. 153–172.

West, T.G., Bradbury, Thomas T.J., 2018. Chapter 3 – 3D Printing: a case of ZipDose® technology – world's first 3D printing platform to obtain FDA approval for a pharmaceutical product. In: Maniruzzaman, Mohammed (Ed.), 3D and 4D Printing in Biomedical Applications: Process Engineering and Additive Manufacturing. Wiley-VCH, pp. 53–79.

Zhang, J., Li, Y., Cai, Y., Ahmad, I., Zhang, A., Ding, Y., Qiu, Y., Zhang, G., Tang, W., Lyu, F., 2022. Hot extrusion 3D printing technologies based on starchy food: a review. Carbohydr. Polym. 294, 119763.

Zhao, Y., Phalswal, P., Shetty, A., Ambrose, R.P.K., 2021. Effects of powder vibration and time consolidation on soft and hard wheat flour properties. KONA Powder and Particle Journal 38, 226–234.

Zhu, S., Vazquez Ramos, P., Heckert, O.R., Stieger, M., van der Goot, A.J., Schutyser, M., 2022. Creating protein-rich snack foods using binder jet 3D printing. J. Food Eng. 332, 111124.